ACS OMEGA

Article

Cite This: ACS Omega 2019, 4, 18035−18048

http://pubs.acs.org/journal/acsodf

Underpinning the Interaction between NO_2 and CuO Nanoplatelets at Room Temperature by Tailoring Synthesis Reaction Base and Time

Dina N. Oosthuizen,*[,†,‡] David E. Motaung,[†,§] André M. Strydom,[∥] and Hendrik C. Swart[†]

[†]Department of Physics, University of the Free State, P.O. Box 339, Bloemfontein ZA9300, South Africa

[‡]DST/CSIR National Centre for Nano-Structured Materials, Council for Scientific Industrial Research, Pretoria 0001, South Africa

[§]Department of Physics, University of Limpopo, Private Bag X1106, Sovenga 0727, South Africa

[∥]Highly Correlated Matter Research Group, Department of Physics, University of Johannesburg, P.O. Box 524, Auckland Park 2006, South Africa

Supporting Information

ABSTRACT: An approach to tailor the morphology and sensing characteristics of CuO nanoplatelets for selective detection of NO_2 gas is of great significance and an important step toward achieving the challenge of improving air quality and in assuring the safety of mining operations. As a result, in this study, we report on the NO_2 room temperature gas-sensing characteristics of CuO nanoplatelets and the underlying mechanism toward the gas-sensing performance by altering the synthesis reaction base and time. High sensitivity of ~40 ppm^{-1} to NO_2 gas at room temperature has been realized for gas sensors fabricated from CuO nanoplatelets, using NaOH as base for reaction times of 45 and 60 min, respectively at 75 °C. In both cases, the crystallite size, surface area, and hole concentration of the respective materials influenced the selectivity and sensitivity of the NO_2 gas sensors. The mechanism underpinning the superior NO_2 gas sensing are thoroughly discussed in terms of the crystallite size, hole concentration, and surface area as active sites for gas adsorption.

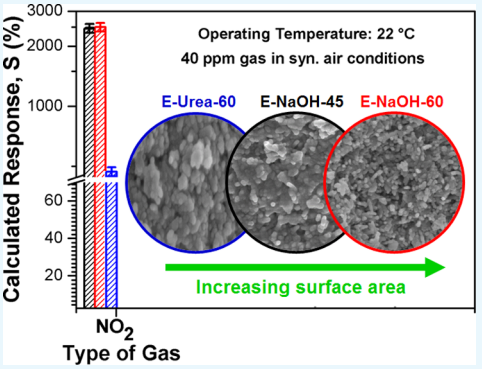

1. INTRODUCTION

The development and implementation of sustainable gas detection systems, that can potentially safeguard the environment, have received a great deal of attention. Gases such as hydrocarbons, carbon monoxide (CO), ammonia (NH_3), hydrogen (H_2), and sulphur dioxide (SO_2) are detrimental to health, an explosion hazard and can even be lethal. Nitrogen dioxide (NO_2) is one of the most common air pollutants from automotive and combustion emissions.[1] It is toxic and harmful to human health in lower concentrations causing serious diseases such as chronic bronchitis, emphysema, and respiratory irritation.[1b,c] Recently, Greenpeace Africa has announced that the largest NO_2 hotspot, across the six continents, is currently located in South Africa. This has reportedly led to numerous deaths and restricted workdays resulting in a total loss greater than US$2.3 billion per year.[2] Therefore, it is crucial to develop high-performance sensors to detect NO_2 gas swiftly and reliably.

For over five decades solid-state metal oxide (MOX)-based gas sensors have been developed and applied because they are small, highly sensitive (detection of different target gases in the ppm to ppb range), and cost-effective compared to classical instrumental analysis.[3] The sensing performance of MOX-based gas sensors strongly depends on the electrical conduction, which is affected by the number of charge carriers and active sites available on the surface, of the sensing material.[4] Large specific surface area and point defects, which promotes adsorption and desorption of oxygen ions and gas atoms from the sensor materials, as well as morphology and crystallographic structures, are factors reported to have an influence on the gas-sensing performance.[5] Most of the gas sensor research thus far was directed toward using n-type MOX semiconductors, such as CeO_2, SnO_2, WO_3, or ZnO for gas sensors.[6] More recently, the focus has shifted to p-type semiconducting and MOX nanocomposite gas sensors.[7] Compared to n-type materials, some p-type gas-sensitive materials have been reported to have significant surface reactivity to oxidizing and reducing gases at lower operating temperatures, which might lead to future advances in low energy consumption gas-sensing devices.[7a,b,8] Cupric oxide (CuO) has attracted a great deal of attention over the last decade because of its wide range of potential applications,[9] including gas sensors.[7f,10] Gas sensors based on CuO nanostructures have exhibited superior sensing perform-

Received: June 24, 2019
Accepted: September 16, 2019
Published: October 23, 2019

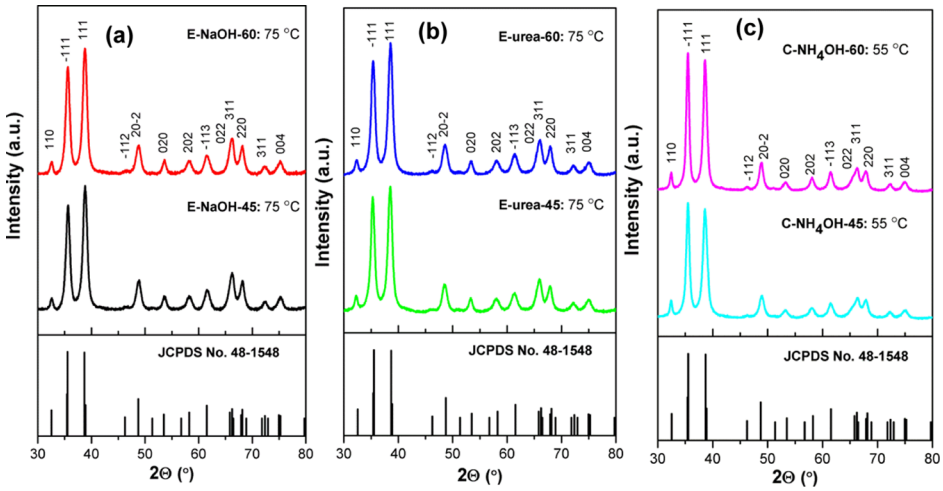

Figure 1. XRD patterns of the as-prepared CuO products, (a) **E-NaOH-45** and **E-NaOH-60**, (b) **E-Urea-45** and **E-Urea-60**, and (c) **C-NH_4OH-45** and **C-NH_4OH-60**.

ances.[7f,10f,g] Enhanced sensor response to NH_3, H_2S, and NO_2 gases have previously been reported for CuO nanostructures below an operating temperature of 200 °C, while sensitivity to volatile organic compound (VOC's) was found above 200 °C.[10e,11]

Previously, we showed that the sensing performance of CuO nanomaterials is dependent on the preparation conditions, that is, reaction temperature and copper ion intermediate. By adjusting these conditions, the material properties including point defects and surface area were advertently changed, resulting in the enhanced sensitivity to NO_2 gas at room temperature.[7f] In this paper, we report on the effect of prolonged reaction times on the subsequent gas-sensing performance of the CuO nanoplatelets. A thorough study on the gas-sensing performance of the nanoplatelet CuO-based gas sensors to various gases, including NH_3, CO, CH_4, NO_2, H_2S, and isopropanol (IPA), at room temperature is investigated. We demonstrate the underlying mechanism toward the enhancement of gas-sensing response by modifying the synthesis reaction base and time.

2. RESULTS AND DISCUSSIONS

2.1. Characterization of the CuO Gas-Sensing Material. CuO nanoplatelets were prepared by the sonochemical method, and the purified CuO products were characterized by X-ray diffraction (XRD), scanning electron microscope (SEM), and high-resolution transmission electron microscopy (HR-TEM). As confirmed by the XRD patterns and indexed according to the JCPDS card no. 48-1548, all as-prepared CuO products obtained after various reaction times (i.e., 45 and 60 min) at 55 and 75 °C in the presence of various bases (**C-NH_4OH-45** and **C-NH_4OH-60** prepared from NH_4OH at a reaction temperature of 55 °C; **E-NaOH-45** and **E-NaOH-60**, and **E-Urea-45** and **E-Urea-60** prepared, at a reaction temperature of 75 °C, from NaOH and urea, respectively) were pure monoclinic-phase, as seen in Figure 1a–c. No characteristic peaks from the precursors and intermediates, such as Cu_2O or $Cu(OH)_2$, was been observed, suggesting that the $Cu(NO_3)_2{\cdot}3H_2O$ and $Cu_2(OH)_2CO_3$ precursors have been completely transformed into CuO. The average crystallite size of the synthesized CuO nanoplatelets was calculated using the Debye–Scherrer formula[12] and the lattice strain (ε), as shown in the Supporting Information, Table S1. The characteristic bands of CuO were observed in Raman spectra at ~280, 330, and 610 cm^{-1}, corresponding to the standard A_g (297 cm^{-1}) and two B_g (345 and 632 cm^{-1}) modes, respectively, further confirming the phase purity of the synthesized CuO nanoplatelets (see Figure S1a–c in the Supporting Information).

The growth mechanism of CuO nanoplatelet products can be explained on the basis of the chemical reactions and nucleation. As previously reported, three synthetic routes were followed to obtain the desired CuO products.[7f] In all three cases, the copper salt precursor, $(Cu(NO_3)_2{\cdot}3H_2O)$, was dissolved in distilled water to form an octahedral copper intermediate complex, $[Cu(H_2O)_6]^{2+}$. The first and the most simple synthetic route included the addition of a high concentration of NaOH solution to the reaction mixture containing $[Cu(H_2O)_6]^{2+}$ producing square-planar complex $[Cu(OH)_4]^{2-}$ ions (ratio of ~2.5:1, OH^- to Cu^{2+}), which is easily transformed to CuO nuclei. During the second and third synthetic routes, the $[Cu(H_2O)_6]^{2+}$ ion complex was transformed to $[Cu(NH_3)_4(H_2O)_2]^{2+}$ with the addition of NH_4OH, and $Cu_2CO_3(OH)_2$ with the addition of urea, respectively. From these subsequent octahedral complex solutions, the high concentration of OH^- anions present from the addition of NaOH mixture resulted in the formation of a $[Cu(OH)_4]^{2-}$ ion complex which led to the formation of the CuO nuclei. Thus, during each of these three synthetic routes, NaOH operates as a pH buffer to control the pH value of the solution. When the critical value of the concentration of the OH^- and Cu^{2+} ions are achieved, the precipitation of CuO nuclei begins. Initially, the CuO nuclei growth takes place by self-aggregation to produce smaller crystallite size CuO nucleus. Further aggregation leads to the formation of CuO nanoplatelets, corresponding to the growth mechanism provided by Cao et al., where the addition of hydrazine hydrate decreased the Gibbs free energy of the reaction system and transformed the 2D nanoleaf to the 3D spherical morphology.[11d]

Figures 2a–f and 3a–i show the SEM and transmission electron microscopy (TEM) images of the platelet-like CuO nanostructures. As shown in Figure 2, the size of the nanoplatelets decreased as the reaction mixture was exposed to a longer reaction time, as seen for **E-NaOH-45** and **E-NaOH-60**, **E-Urea-45** and **E-Urea-60**. The nanoplatelets structural units of **C-NH_4OH-45** and **C-NH_4OH-60** were

DOI: 10.1021/acsomega.9b01882
ACS Omega 2019, 4, 18035–18048

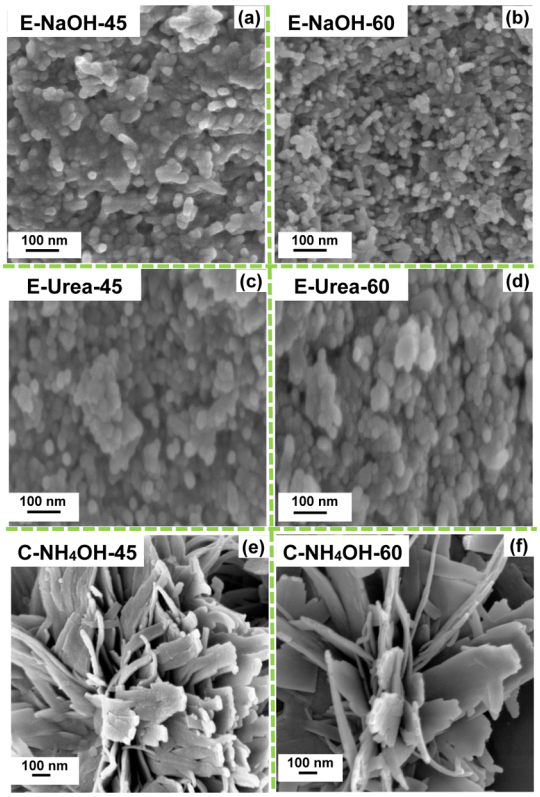

Figure 2. (a–f) SEM micrographs at high resolution for of the six the CuO products prepared from different reaction bases and different reaction times.

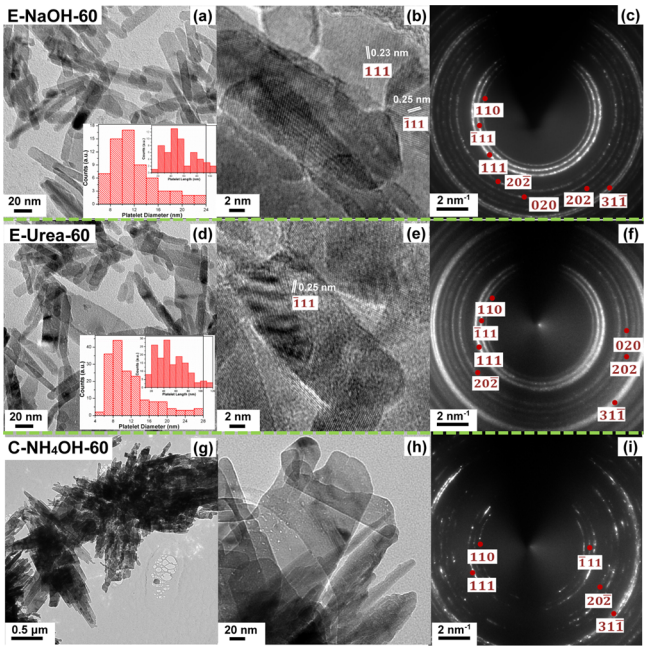

Figure 3. (a–f) High-resolution TEM images show the platelet-like nature (inset is the size distribution of the platelet diameter and length), the lattice fringes, and the corresponding SAED patterns of **E-NaOH-60** and **E-Urea-60**. (g,f) Typical low- and high-magnification TEM images with the corresponding SAED pattern (i) of **C-NH_4OH-60**.

arranged in flower-like structures in the presence of NH_4OH (see Figure 2e,f). The length of the nanoplatelets was also affected (i.e., length decreases) with the increase in reaction times. As shown in the size distribution of **E-NaOH-60** and **E-Urea-60** (Figure 3a,d insets), the length and diameter of the nanoplatelets are affected by the change in base, displaying an average diameter and length of approximately 8–12 and 40–80 nm, respectively. More detailed crystallographic analyses on the CuO nanoplatelets were performed by selected area electron diffraction (SAED) and HR-TEM analysis. The *d*-spacing of the CuO lattice was found to be 0.23 and 0.25 nm corresponding to the $(\bar{1}11)$ and (111) crystal planes of CuO crystal planes of CuO (see Figure 3b,e). The SAED patterns for **E-NaOH-60** and **E-Urea-60** show the diffused Debye rings, denoting that the diameter of the platelets is small (see Figure 3c,f). The $(\bar{1}11)$, (111), (110), and (200) crystal planes observed in the SAED pattern confirm the monoclinic phase of the CuO nanoplatelet products. Because of the large nature of the nanoplatelets of **C-NH_4OH-60**, the SAED pattern predominantly reveals brighter Debye rings with discrete spots, denoting that the CuO flower-like structures are more polycrystalline in nature, as seen in Figure 3g–i. These observations are consistent with the XRD patterns showed in Figure 1a–c.

By varying the reaction times, the surface areas and pore volumes as determined by BET surface analyses were affected. Analyses confirmed the surface area and pore volume of **E-NaOH-60** was the largest, compared to the other as-prepared CuO products (see Figure S2 and Table S2 in the Supporting Information). As seen in Figure 4a–c, there is an inverse correlation between the BET surface area and average crystallite sizes determined from the peaks associated with the (111) and $(\bar{1}11)$ XRD planes, as a function of reactions time. Experimentally, it was observed that extending the reaction times to above 60 min led to a decrease in the surface area.

X-ray photoelectron spectroscopy (XPS) analyses were employed to understand the chemical state and shift of the oxygen and copper atoms in the CuO products, as seen in Figures 5 and 6. The spectra, Figure 5a–f, reveal doublet peaks located at around ∼933.1 and ∼953.3 eV which can be assigned to the binding energies of Cu $2p_{3/2}$ and $2p_{1/2}$, characteristic to the values associated to Cu^{2+}. The two overlapping satellite shake-up peaks are at ∼941.4 and ∼943.9 eV; and a strong satellite shake-up peak is at ∼962.4 eV, further confirming the presence of Cu^{2+}.[13] Both CuO and Cu_2O can be distinguished by the binding energy of Cu $2p_{3/2}$ and Cu $2p_{1/2}$ in the Cu 2p XPS spectra because of the difference of ∼1 eV for CuO and Cu_2O.[13a,b,14] The O 1s core level spectra (see Figure 6a–f) of the six samples contain three peaks: a main peak and smaller peak (blue and light blue), O_i, at ∼529.3 and O_{ii}, at 531 eV, where O_i is the O^{2-} binding with Cu^{2+} in the crystal lattice, the O_{ii} peak is caused by weakly adsorbed species, which include OH^- or O_2^{2-} species from the environment and the smallest peak, and O_{iii} (light pink) at ∼532 eV is associated with weakly adsorbed oxygen species.[15] The O_{iv} peak (light green) found at ∼533 eV is associated with the compensation of deficiencies in the subsurface or oxygen-vacancy species.[15]

Photoluminescence (PL) studies were conducted at room temperature, with an excitation wavelength of 325 nm, to determine the amount of point defects in the CuO products. The overlaid PL spectra of the all six as-prepared products are shown in Figure 7a_1–c_1, with the convoluted spectra of **E-NaOH-60**, **E-Urea-60** and **C-NH_4OH-45** shown in Figure

DOI: 10.1021/acsomega.9b01882
ACS Omega 2019, 4, 18035–18048

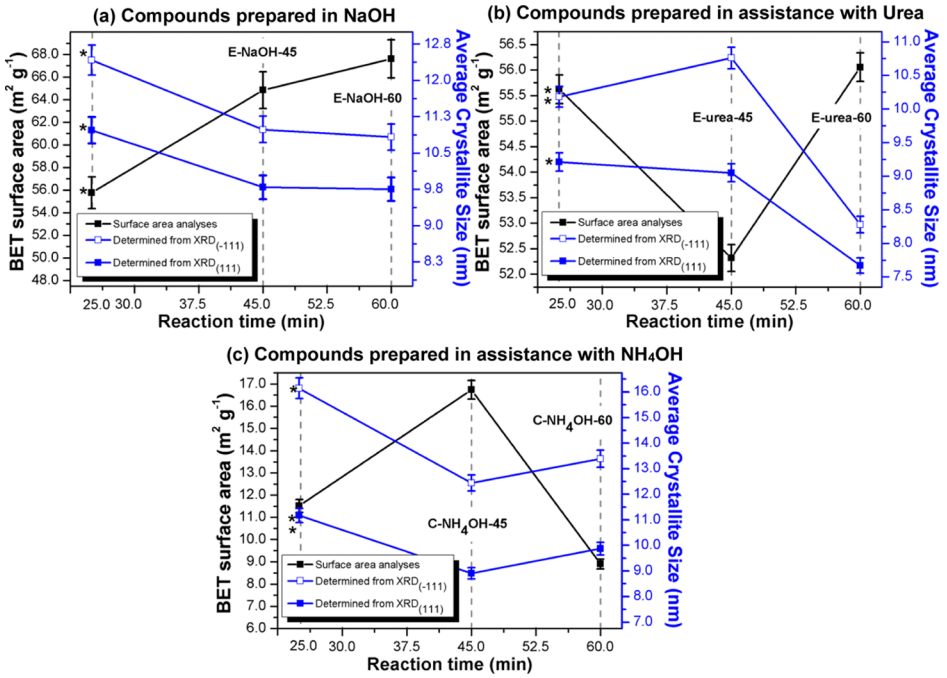

Figure 4. BET surface area and average crystallite size of the as-prepared CuO products as a function of reaction time. Note the compounds marked with the asterisk (*) are from our related work[7f] **E-NaOH**: 75 °C, **E-Urea**: 75 °C, and **C-NH_4OH**: 55 °C and the line visible in (a–c) are not experimental data; it is used to guide the reader. "Adapted and reprinted from *Sensors and Actuators B: Chemical*, Vol. 266, D.N. Oosthuizen, D.E. Motaung, H.C. Swart, in depth study on the notable room-temperature NO_2 gas sensor based on CuO nanoplatelets prepared by sonochemical method: comparison of various bases, Pages 761-772., Copyright (**2019**), with permission from Elsevier."

7a–c_2. The band at 410 nm (i.e., ∼3.0 eV) corresponds to the band-edge emission. The defects peaks associated with possible transition vacancy of oxygen (V_o) and interstitial oxygen (O_i) in the blue-violet region (440–475 nm or 2.61–2.82 eV) of the spectra are visible in the PL spectra, as shown in Figure 7a–c_2. The defect peaks related to singly ionized oxygen vacancy (V_o^+) and both O and Cu interstitial (O_i and Cu_i) deficiencies are visible in the green region (between 475 and 575 nm or 2.15 and 2.82 eV) of the PL spectra. The peak located at the red region between 575 and 700 nm (i.e., 2.15 and 1.77 eV) is associated with doubly ionized oxygen vacancies (V_o^{++}), for **E-Urea-60**.[16]

To further study the magnetic properties of the CuO products, we carried out magnetization measurements at 10 K under a maximum applied magnetic field of 10 000 Oe with a by vibrating sample magnetometer (VSM). Figure 8 displays the magnetization versus magnetic field (M–H) curves for the CuO nanostructures. The small hysteresis loop observed at lower field indicates the **E-NaOH-45** containing both ferromagnetic (FM) and paramagnetic (PM) features (see Figure 8a). Such behavior is also observed for the **C-NH_4OH-60** (see Figure 8d). Although the FM contribution exists for the **E-NaOH-60**, a superimposed negative contribution turns out to be dominant (see Figure 8b). This diamagnetic temperature-independent involvement may originate from filled electronic d-shell of the Cu_2O layer. No peaks related to Cu_2O were observed during XRD analyses (see Figure 1a); however, the presence of Cu_2O was confirmed by XPS analyses (see Figure 5b). This diamagnetic contribution to the total magnetization becomes dominant at higher fields. A clear hysteresis loop is witnessed for **C-NH_4OH-45** (see Figure 8c). Strong PM signals are evident for **E-urea-45** and **E-urea-60** (see Figure 8e,f); corresponding to the XPS analyses where large amounts of Cu^{2+} ions are observed in the products (see Figure 5c,d). **C-NH_4OH-45** showed the largest saturation magnetization of (i.e., 0.1 emu/g), while saturation magnetization for the **E-urea-60** was too small to detect.

2.2. Gas Sensing Analyses of CuO Nanomaterials.

2.2.1. CuO Sensing Performance. The performance testing further include exposing the sensors to various concentrations of preselected gases [test gases including NH_3, CO, CH_4, NO_2, H_2S and IPA] in dry air and humidity conditions, at room temperature. These gases were selected as cross-sensing gases because recent reports showed that South Africa is currently one of the largest emitters of NO_x, while other gaseous emissions of concern include the presence of NH_3, CO, and other sulphur-related compounds. Even though VOC's emissions in the South African atmosphere are currently limited, the sensors were exposed to one VOC gas (i.e., IPA gas) for future reference. The calculated response, S, is defined as $((R_a - R_g)/R_g) \times 100\%$) in the oxidizing gas (i.e., NO_2) atmosphere, where R_a and R_g are resistance of the sensor in air and in testing gas atmosphere, respectively.[17] For the initial gas selectivity screening, each gas concentration was pulsed for 5 min, followed by synthetic air for 5 min.

Selectivity is a vital parameter for gas-sensing application. Such selectivity between NO_2 and other interferences gases such as IPA, NH_3, H_2S, CO, and CH_4 remains the fundamental challenges for practical NO_2 MOX-based nanosensors. The gas-sensing responses of the CuO nanostructures prepared using various bases at different reaction times were tested toward various gases at room temperature, and the results are presented in Figure 9. As displayed in the histogram, the **E-NaOH-45**, **E-NaOH-60**, and **E-urea-60** show improved response to NO_2 gases compared to other gases. Sensors **E-NaOH-45** and **E-NaOH-60** showed response of values of approximately 2465 and 2498% to 40 ppm NO_2 gas, respectively, at room temperature in dry air conditions.

DOI: 10.1021/acsomega.9b01882
ACS Omega 2019, 4, 18035–18048

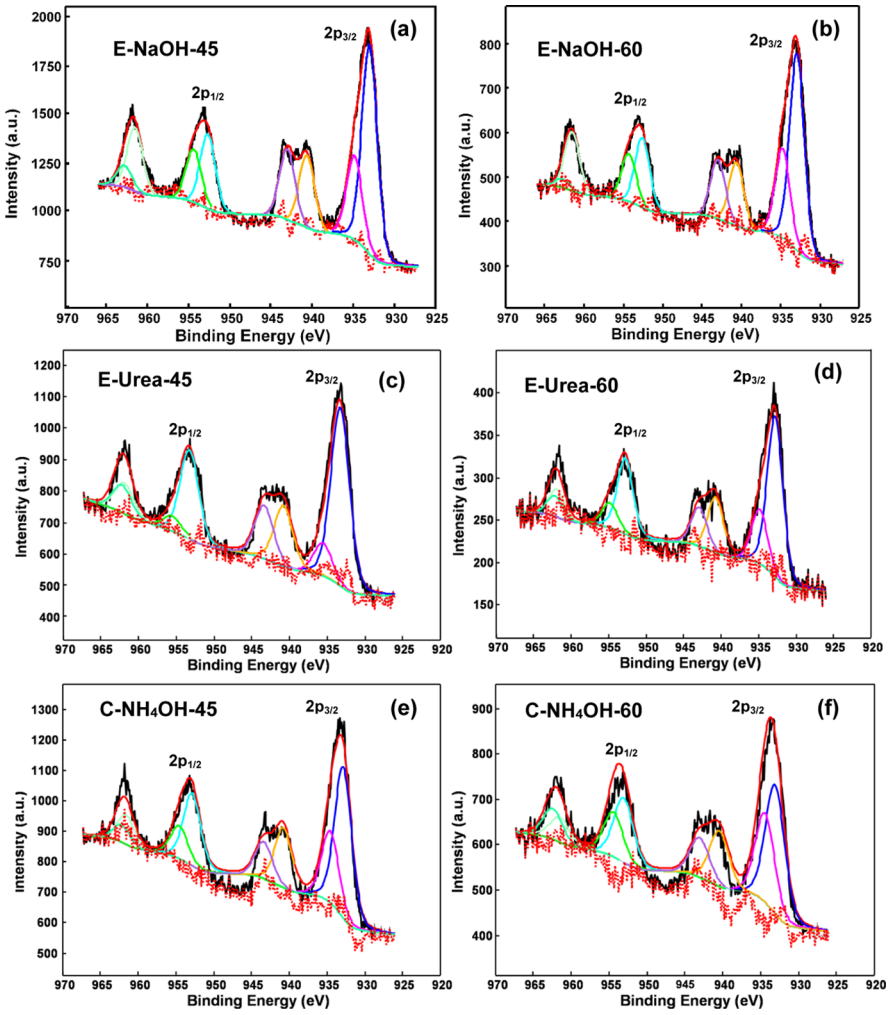

Figure 5. (a–f) Chemical shift of the copper peaks of in XPS analyses.

These findings clearly show that the sensor response to NO_2 gas is reaction base and time dependent. None of the sensors showed a response to H_2S or CO gas. All relevant sensors' performance data related to CH_4 sensing are showed in the Supporting Information (see Figures S7 and S8). To be specific, it is important to note that large drifts in sensor current (i.e., sensor instability) were observed in the presence of CH_4 gas, which in turn made it difficult to determine the maximum response values. By ignoring the drift, the maximum response values of between 1700 and 2100 was estimated for sensors **E-NaOH-45** and **E-NaOH-60**, to 40 ppm CH_4.

2.2.2. NO_2 Sensing in Various Atmospheres. The dynamic curves are provided in terms of resistance and are displayed in logarithmic scale in order to allow for a better comparison between the changes of the sensor signals (relative change of the resistance). The high response of **E-NaOH-45-**, **E-NaOH-60-**, and **E-urea-60**-based gas sensors to NO_2 gas is attributed to the presence of weakly adsorbed oxygen species and the higher relative concentration of point defects (confirmed by XPS and PL analyses, see Figures 6 and 7, respectively) which act as favorable adsorption sites for chemisorbed oxygen species to participate in the reaction than that of other CuO nanomaterials. Our previous work and that of other researchers have shown that defects have a direct influence on the sensing performance of the materials.[7f,18] The **E-NaOH-60**-based gas sensor is considered as the superior performing NO_2 gas-sensitive material because it showed a response to lower concentrations (i.e., 5 ppm) of NO_2 gas, compared to that of **E-urea-60**, as seen in Figures 10 and 11. As expected, p-type conductivity was observed for the **E-NaOH-45-**, **E-NaOH-60-**, and **E-urea-60**-based gas sensor products in NO_2 gas conditions (see Figures 10 and 11). A large drift in sensor resistance (see Figure 10a,b) was observed, which was can normally attributed to low rate of diffusion of gas molecules away from the surface of the sensor at low operating temperatures. However, at higher NO_2 concentrations, the sensors recover quicker than at lower concentrations, irrespective of the operating temperature. The trend occurs irrespective of the presence of humidity (see Figure 10b,c). The relationship between the sensor drift and sensor response of **E-NaOH-60** over a period of 12 h can be seen in Figure S4, Supporting Information, thus leading us to conclude that at lower concentration the NO_2 molecules chemically bond to the active sites on the surface of the sensing layer. At higher concentrations, however, a combination of chemi- and physisorption occurs because the NO_2 molecules are competing for the same active sites. Prolonging the duration of the gas cycles (see Figure S5, Supporting Information) also proved to be ineffective. The interaction on the gas–solid interface is dependent on the competition between the oxidizing gas and the water vapor for the preadsorbed oxygen species.

DOI: 10.1021/acsomega.9b01882
ACS Omega 2019, 4, 18035–18048

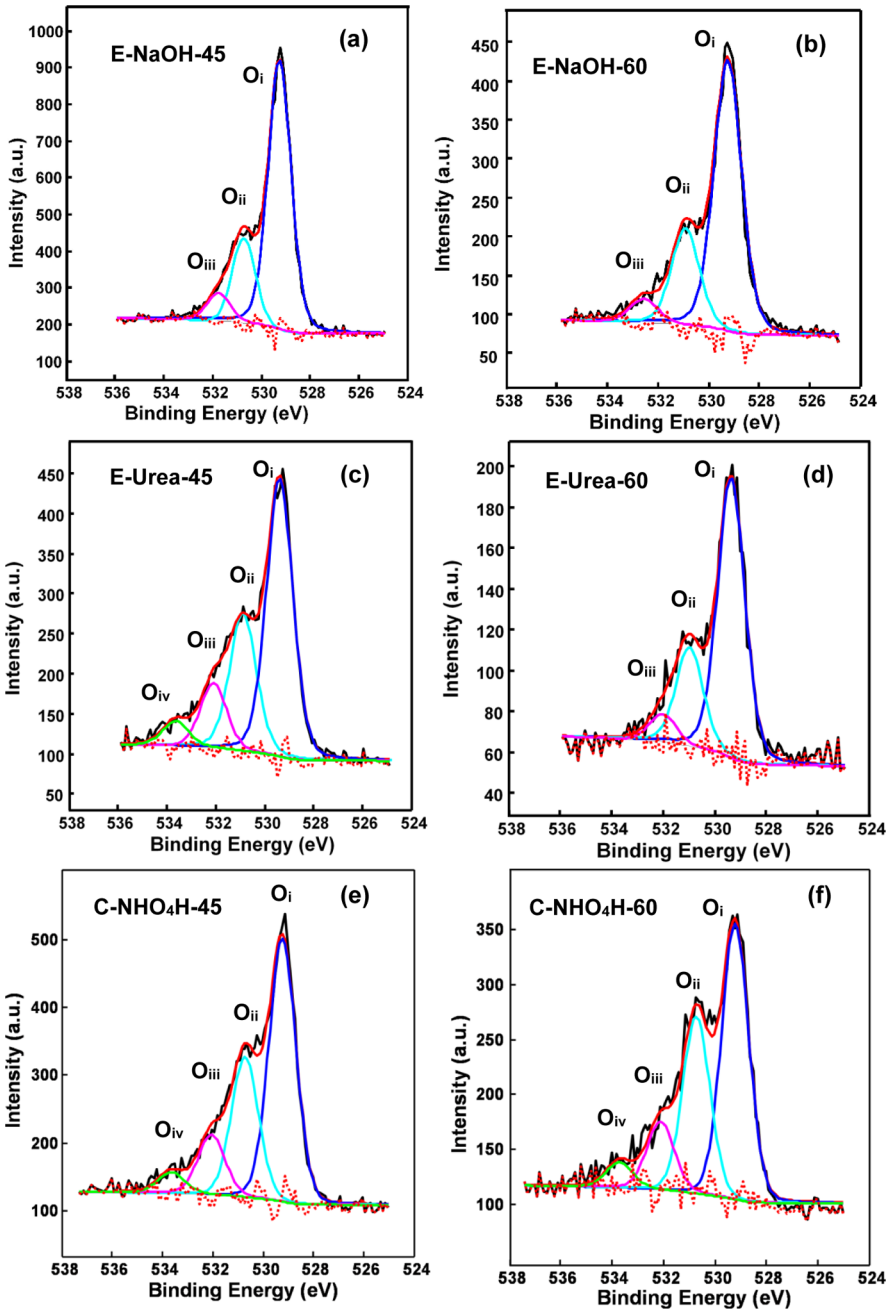

Figure 6. (a–f) Chemical shift associated with the oxygen peak found in the CuO products.

During the exposure of sensor **E-urea-60** to four cycles of 40 ppm NO_2, limited drift in sensor resistance is observed compared to that of the sensor in varying concentrations (see Figure 11a,b). This can be ascribed to the prolonged duration of the gas cycles which allowed the gas molecules efficient time to diffuse away from the surface of the sensor. A decline in sensor resistance was observed after the sensor was exposed to NO_2 in humid conditions (as seen in Figure 11c). The drift in resistance of the **E-urea-60** sensor in the presence of humidity can be attributed to the gradual formation of stable chemisorbed OH-groups at the oxide surface for prolonged exposure.[19] Compared to dry air condition, a decrease in the sensor response for **E-urea-60** was observed in testing conditions with more moisture present (see Figures 9 and 11d).

2.2.3. Stability of Sensors in the NO_2 Atmosphere. When exposing the **E-NaOH-45**, **E-NaOH-60**, and **E-urea-60** sensors to NO_2 in dry air and humidity conditions after aging for a year, more complex gas-sensing performances are observed (see Figures 12 and S7 in the Supporting Information). An increase in initial sensor resistance (i.e., before the target gas was introduced) was observed for the sensors (see Figure 10a,b compared to Figure 12a,b), which can be ascribed to the presence of additional adsorbed species, like H_2O and O^-, on the surface of the sensors leading to overall increase in sensor conductivity. Under dry air conditions, a more pronounced drift in both the sensors' resistance was observed (see Figure 12a). The NO_2 species is most likely to now bond to the additional active sites on the surface of the sensing layers. In the scenario where the sensing performance is tested in dry air conditions (see Figure 12a),

DOI: 10.1021/acsomega.9b01882
ACS Omega 2019, 4, 18035−18048

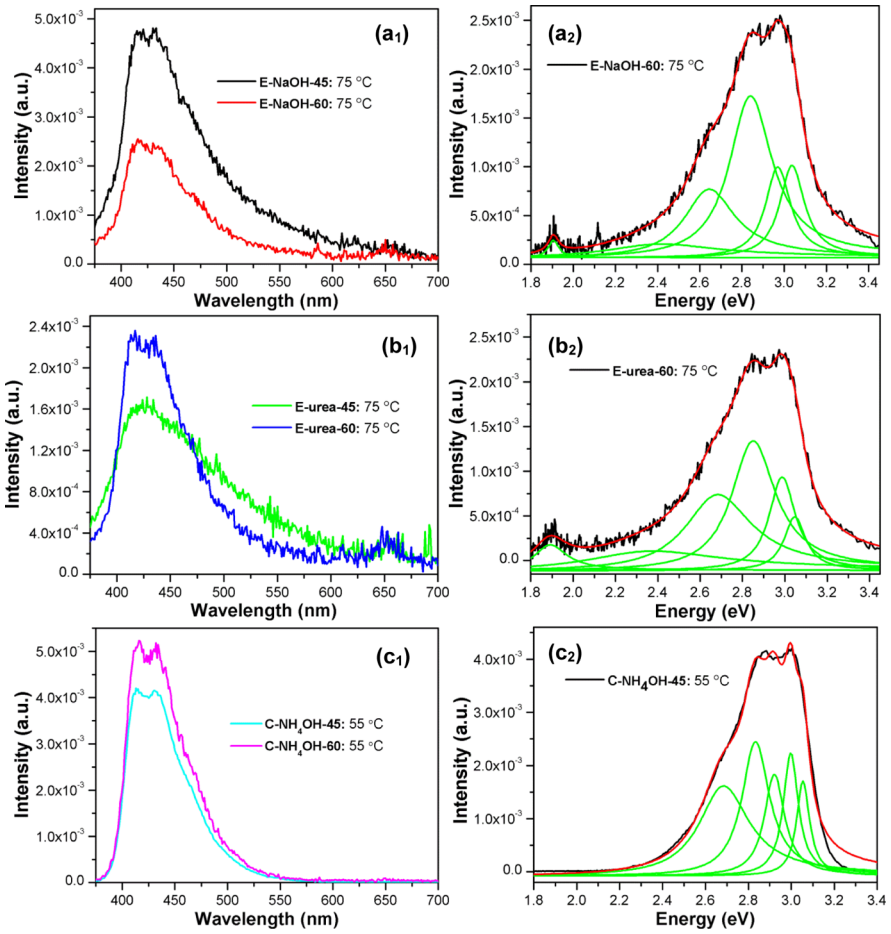

Figure 7. (a_1–c_1) Overlaid PL spectra of all of the CuO products prepared in the presence of NaOH, NH_4OH and urea, with the convoluted spectra of **E-NaOH-75**, **C-NH_4OH-45**, and **E-Urea-60** (a_2–c_2).

prolonging duration of the gas cycles even more (i.e., 20 and 20 min: gas in and gas out) or heating the sensors to above 100 °C between gas NO_2 gas cycles may remove the additional species, thus regenerating (restore) the sensors to their original condition. However, enhanced sensing performance for **E-NaOH-45** and **E-NaOH-60** was observed in the presence of humidity (see Figure 12b,c). Because of the likelihood of additional adsorbed species present on the surface of the sensing layer, the most likely scenario is the reaction of preadsorbed oxygen, namely O^-, with water resulting in the formation of terminal hydroxyl groups (i.e., the cause of more distinct the sensor drift in more humid atmosphere). Thus, the interaction mechanism is now dependent on the competition between the oxidizing gas and the water for the additional preadsorbed oxygen species.

2.2.4. Gas-Sensing Mechanism Arising from the Material Properties. The manner in which the conduction occurs in the MOX sensing layer is important for the magnitude of the sensor signal (sensor response).[20] The general sensing mechanisms of the semiconductor gas sensors are based on the ionosorption and oxygen-vacancy models.[5b] The adsorption and desorption of test gas on the surface of the CuO-based gas sensor leads to the changes of electrical resistance and directly affect the response to the test gas. In general, the gas-sensing response of MOX-based gas sensors can be described as follows

$$S - 1 = a\,C^b \tag{1}$$

where a and b are constants, S is the response of sensor, and C is the concentration of target gas. The value of b is normally from 0.5 to 1 which depends on the charge of the surface species and stoichiometry of the elementary reactions on the sensor surface. The b value is 0.5 when the adsorbed surface oxygen ion is O^{2-}, and the b value is between 0.5 and 1 or just above 1 when the adsorbed surface oxygen ion is O^-. Therefore, the oxygen species adsorbed on the surface of the gas sensor can be deduced by the b value. At a certain working temperature, eq 2 can be rewritten as

$$\log(S - 1) = b \log(C) + \log a \tag{2}$$

There is a linear relation between $\log(S-1)$ and $\log(C)$, and b is the slope of the linear function. Figure 13a shows the relationship between the response of **E-NaOH-45** and **E-NaOH-60**- and **E-NaOH-60**-based sensors and the NO_x concentration, and the corresponding curve of $\log(S-1) \approx \log(C)$ is shown in Figure 13b. The calculated b is 1.0 and 1.139, respectively, which signifies that O^- species are adsorbed on the surface of the sensing layers.

It is suggested that in the case of these CuO sensors, the NO_2 firstly reacts with the available adsorbed O^- species forming NO_2^-(ads) species. Then, a hole-accumulation layer is created at the boundaries of the CuO nanograins by chemisorption of NO_2. The generation of holes makes the p-type CuO nanoplatelets more conductive.

$$NO_2(g) \rightarrow NO_2^-(ads) + h^+ \tag{3}$$

DOI: 10.1021/acsomega.9b01882
ACS Omega 2019, 4, 18035−18048

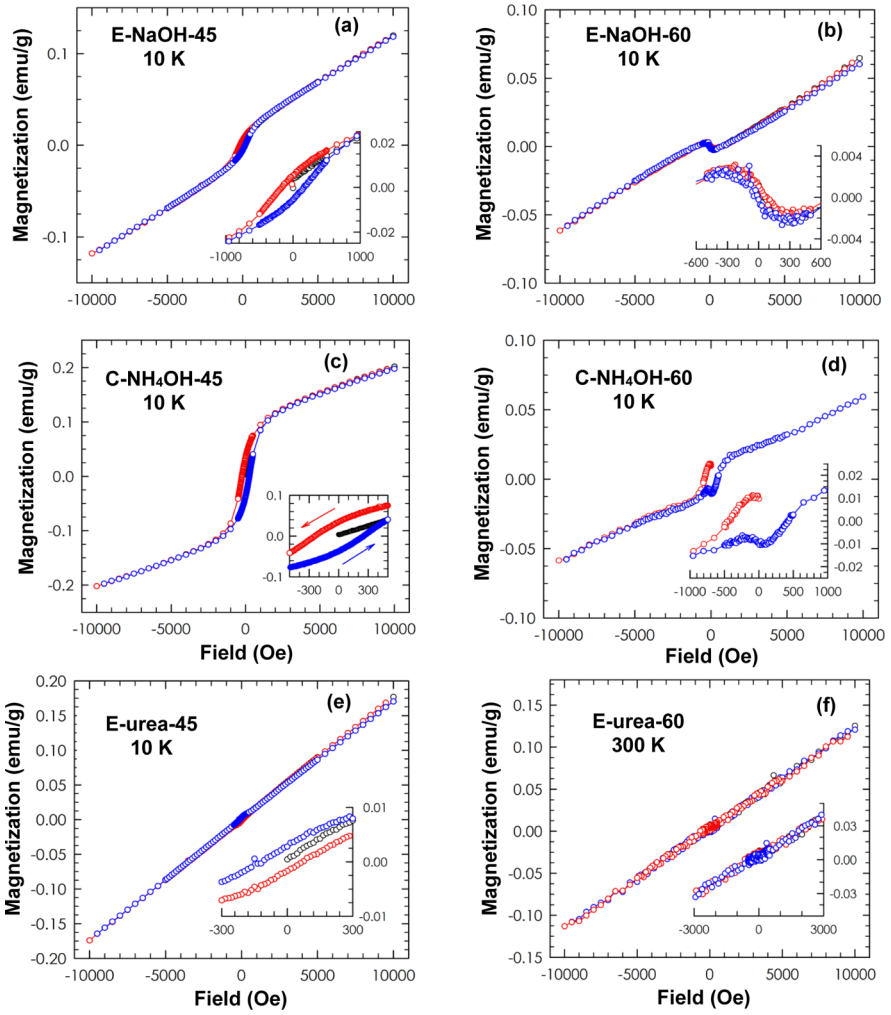

Figure 8. Magnetization versus magnetic field ($M-H$) curves of CuO nanoplatelets measured at (a–e) 10 and (f) 300 K.

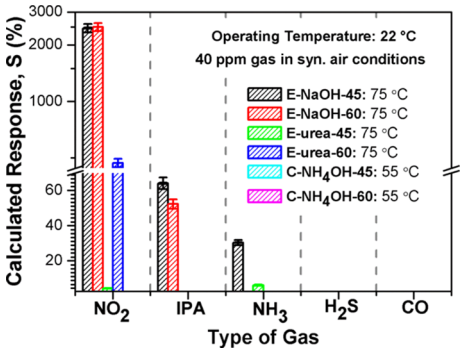

Figure 9. Selectivity histogram of as-prepared CuO nanostructures exposed to 40 ppm CH_4, H_2S, CO, NH_3, and NO_2 gas in dry air at room temperature.

When the flow of NO_2 gas is stopped, the adsorbed NO_2^-(ads) species evaporates, leaving behind the captured electrons in the p-type CuO and decreasing the hole density by electron–hole compensation, resulting in the change in resistance. If however the NO_2^-(ads) species does not evaporate or diffuse away from the surface, no electron is donated back into the CuO bulk; thus, the hole density is not decreased (i.e., drift in sensor resistance is observed).

For the aged sensors, the surface chemisorbed O^-(ads) and NO_2^-(ads), as well as their interactions, have a significant impact on the sensing properties because there is more O^-(ads), as illustrated by the following reactions.

$$O_2(g) + 2e^- \rightarrow 2O_2^-(ads) \quad (4)$$

$$NO_2(g) + e^- \rightarrow NO_2^-(ads) \quad (5)$$

$$NO_2(g) + 2O^-(ads) \rightarrow NO_2^-(ads) + O_2(gas) + e^- \quad (6)$$

As is known, the fundamental principle of gas-sensing MOX materials depends on the change in the resistance (or conductivity) in the sensor's circuit when exposing it to different atmospheres (i.e., different gases). It is established that the gas-sensing performance is influenced by many factors, such as the charge carrier concentration on the surface of the sensing materials, morphology, and large surface-to-volume ratio of the sensing materials.[20,21] In the present study, the variations in charge carrier concentrations and morphology were found to change the gas-sensing characteristics of the CuO nanostructures. To get a further indication of the factors that influenced the NO_2 gas-sensing performance of **E-urea-60**, **E-NaOH-45**, and **E-NaOH-60**, in dry air conditions, their calculated NO_2 response at 40 ppm was compared to the crystallite size, surface area, carrier concentration (as seen in

DOI: 10.1021/acsomega.9b01882
ACS Omega 2019, 4, 18035−18048

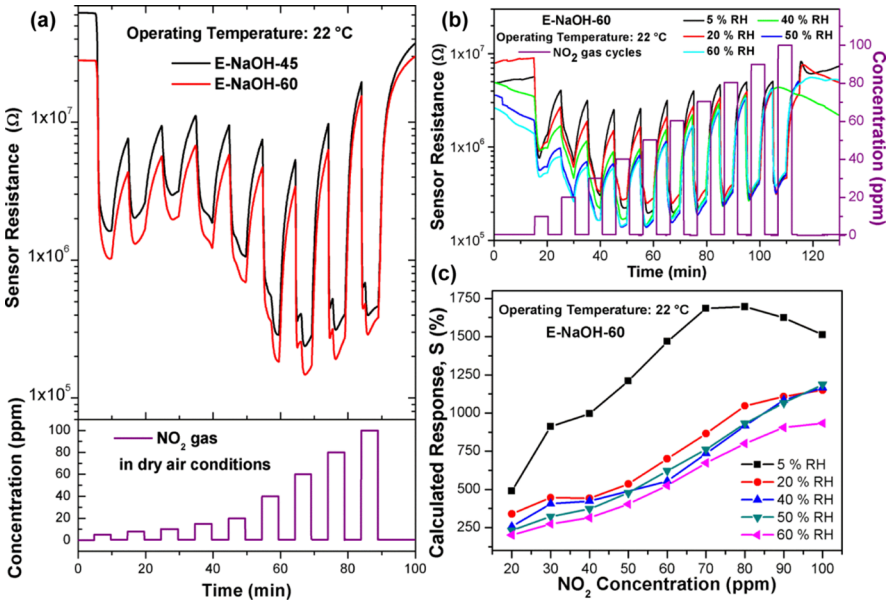

Figure 10. (a) Dynamic resistance curves of the **E-NaOH-45** and **E-NaOH-60**, extracted from different NO_2 concentration cycles and (b,c) the dynamic resistance curve and calculated response (S) variation of **E-NaOH-60** to NO_2 concentrations ranging from 20 to 100 ppm in various relative humidity (%) at room temperature. *Note: the lines visible in (c) are not experimental data; it is used to guide the reader.

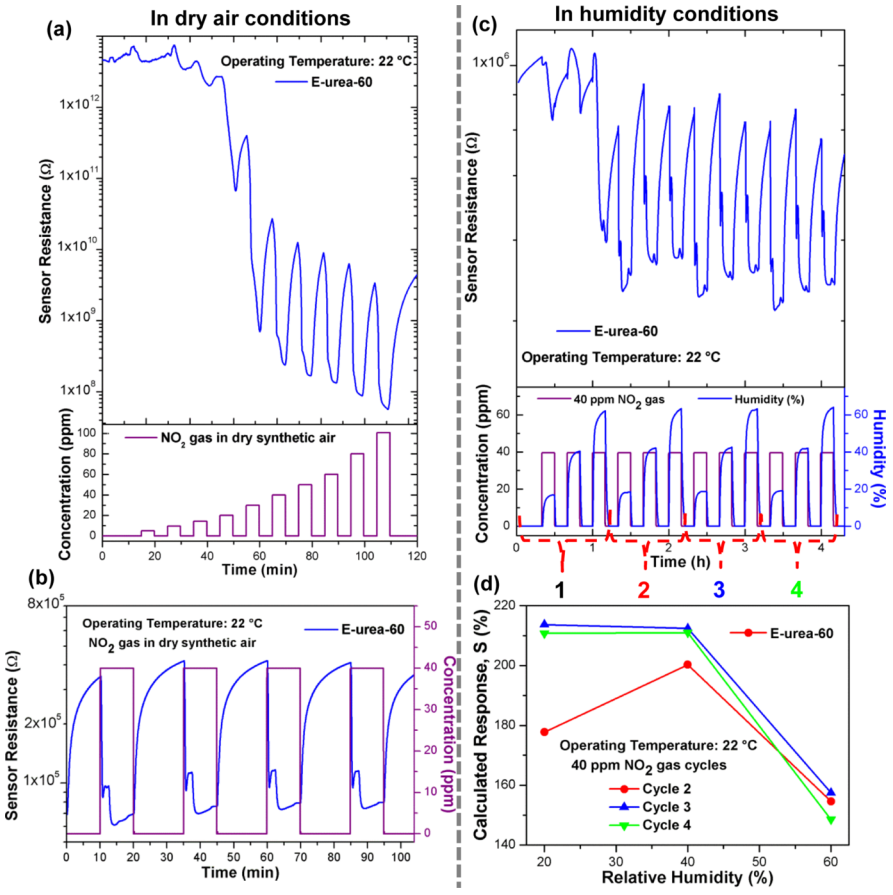

Figure 11. (a) Dynamic resistance curves of **E-urea-60**, extracted from different NO_2 concentration cycles and (b,c) 40 ppm NO_2 gas cycles in dry synthetic air and various relative humidity (%) conditions at room temperature. (d) Calculated response, S, of **E-urea-60** to 40 ppm NO_2 in various (RH %) conditions at room temperature. *Note: the lines visible in (d) are not experimental data; it is used to guide the reader.

the Supporting Information, Figure S3: Hall-effect analyses) and defects (determined by PL and XPS analyses) as seen in Figure 14a−d. From this comparison, it is apparent that the enhanced response of **E-urea-60** and **E-NaOH-45**, to NO_2 gas, respectively, was mostly influenced by the crystallite size, surface area, and the carrier concentration of the sensing

DOI: 10.1021/acsomega.9b01882
ACS Omega 2019, 4, 18035−18048

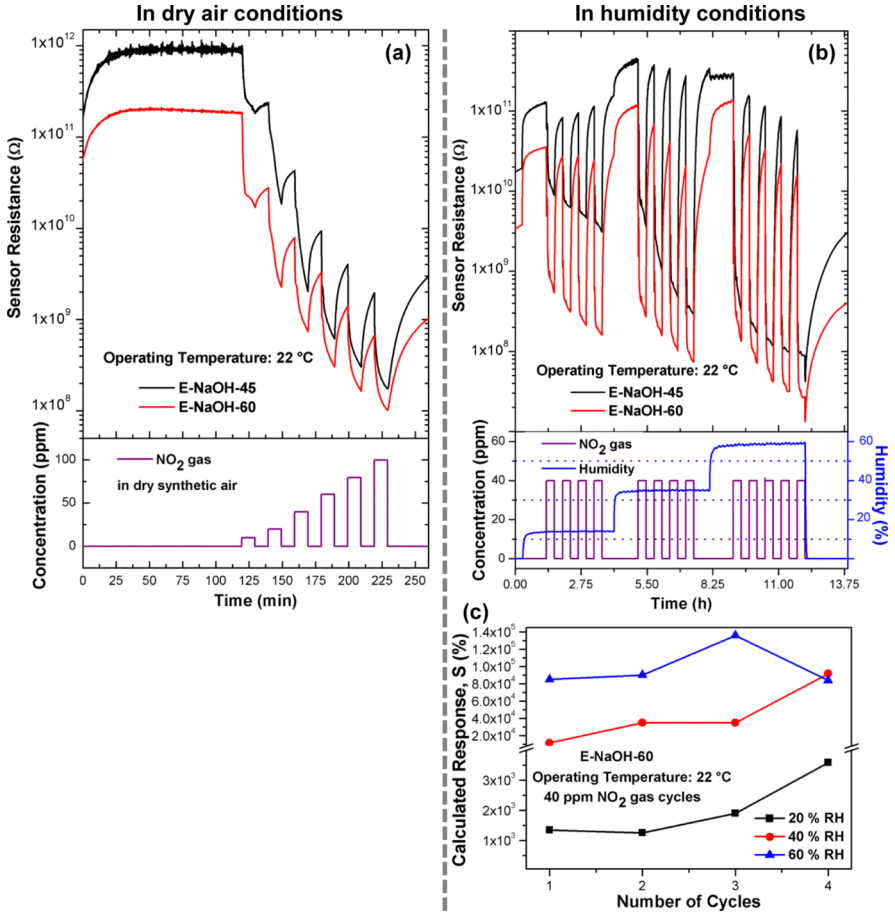

Figure 12. (a) Dynamic resistance curves of **E-NaOH-45** and **E-NaOH-60**, extracted from different NO_2 concentration cycles and (b) 40 ppm NO_2 cycles in dry synthetic air and various RH (%) conditions at room temperature. (c) Calculated response of **E-NaOH-60** to 40 ppm NO_2 gas at various RH (%).*Note: the lines visible in (c) are not experimental data; it is used to guide the reader.

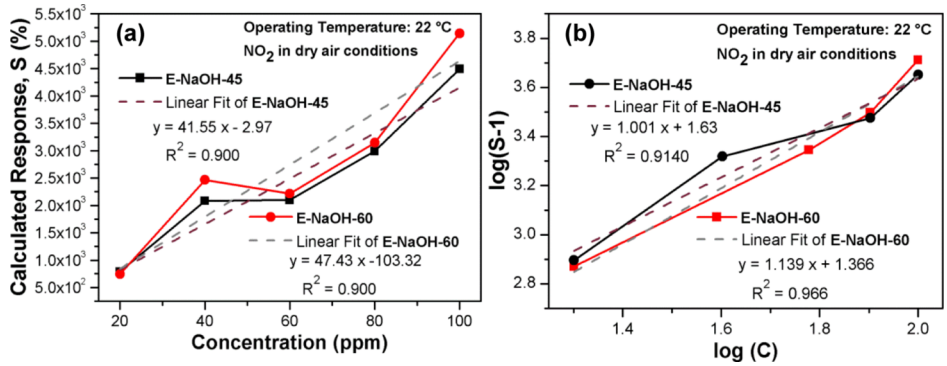

Figure 13. Relationship between (a) calculated response, S, of sensors **E-NaOH-45** and **E-NaOH-60** and the NO_2 concentration at room temperature (22 °C) and (b) corresponding $\log(S-1)$–$\log(C)$ curves.

materials. To be specific, the largest surface area of 67.6 $m^2\ g^{-1}$ by **E-NaOH-60** showed an enhanced NO_2 gas sensitivity with a response of 2498% at 40 ppm, followed by **E-NaOH-45** with a response of 2465% and a surface area of 64.8 $m^2\ g^{-1}$. As the crystallite sizes decreased, the gas-sensing response toward NO_2 gas decreases, denoting that in this case (taking all of the material properties into account) the optimum grain size contributing is 9.7 nm. A previous report has disclosed that the performance of the sensing can be enhanced by manipulating the size of the nanostructures to a critical value of approximately 14 nm.[22] The gas-sensing performance of similar CuO nanostructures, such as nanoleaves and platelet-like building blocks arranged as hierarchical structures, were reported to be selective to VOC's at higher operating temperatures.[10f,11d] Selectivity to NO_2 gas was reported for chromium-doped CuO nanorods at 250 °C, by Lee et al.[23] Limited cases were reported where undoped CuO nanostructure-based gas sensors showed selectivity to NO_2 gas at room temperature;[7f,24] however, other studies include the enhanced NO_2 response of NiO nanosheets[5a,8b] and at room temperature.[8b]

DOI: 10.1021/acsomega.9b01882
ACS Omega 2019, 4, 18035−18048

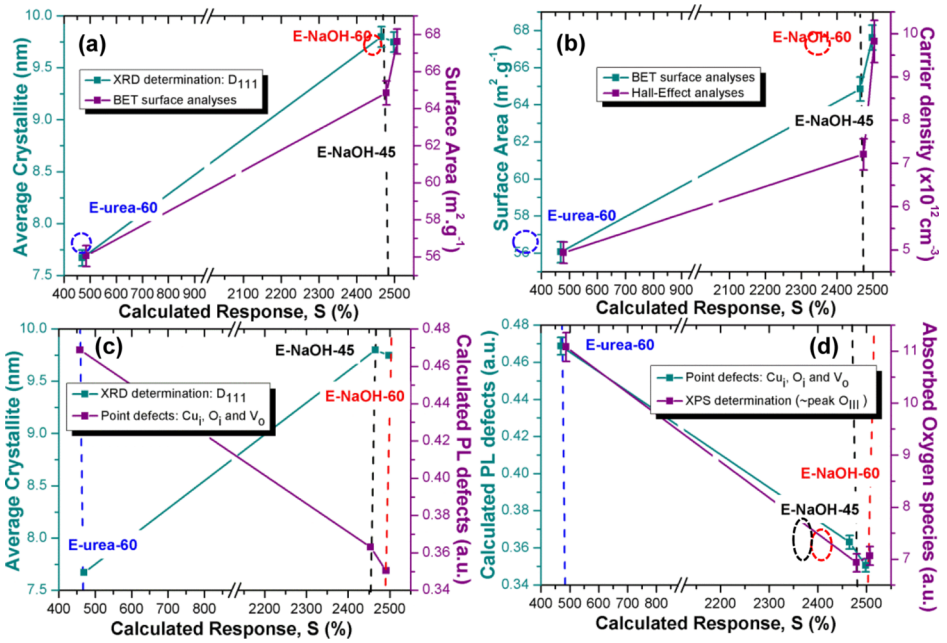

Figure 14. Relationship between the crystallite size, surface area, carrier concentration, defects, and the NO_2 gas-sensing response of **E-NaOH-45**, **E-NaOH-60** and **E-urea-60** (a–d) *Note: the blue and black lines visible in (a,b) are not experimental data; it is used to guide the reader.

3. CONCLUSIONS

Various CuO nanoplatelets were successfully prepared and characterized, before being subjected to gas-sensing performance analyses at room temperature (22 °C) in dry and humid conditions. Both CuO products, prepared at 75 °C for 45 and 60 min in the presence of NaOH, and urea (**E-NaOH-45**, **E-NaOH-60** and **E-urea-60**), showed promise as NO_2 gas sensors, respectively. **E-NaOH-60**, with an average crystalline size of 9.7 nm and largest surface area of 67.6 m^2 g^{-1} and highest carrier concentration, showed an enhanced response of 2498%, while **E-urea-60** (i.e., crystallite size of 7.7 nm and surface area of 56.1 m^2 g^{-1}) showed a smaller response of 469% to 40 ppm of NO_2 gas at room temperature in dry air. This could be attributed to the much larger specific area, the more active sites and the more abundant hole concentration provided by the **E-NaOH-60** nanoplatelets. This finding contributes to the research and development of NO_2 selective p-type MOX-based gas sensor operating at room temperature.

4. EXPERIMENTAL SECTION

4.1. Materials. All reagents were of analytical grade and used as purchased from Sigma-Aldrich. The NH_3, CO, H_2S, NO_2 and CH_4 gases were purchased from AFROX, South Africa.

4.2. Preparation of CuO Nanostructures. As shown in ref 7f, the CuO powders, **E-NaOH**: 75 °C, **C-NH_4OH**: 55 °C, and **E-Urea**: 75 °C, were prepared under specific reaction conditions and exhibited the best gas-sensing performance. During this study, the same preparation method used in ref 7f was followed, under the relevant reaction temperatures, that is, 55 and 75 °C; however, the reaction times were prolonged to 45 and 60 min in this case. Forgoing the chosen notation, resulting CuO products were denoted as **E-NaOH-45** and **E-NaOH-60**, according to the reaction temperature (75 °C), time, and the base used (NaOH). Thus, in the cases where NH_4OH was used in the preparation of CuO nanostructures, the products were denoted as **C-NH_4OH-45** and **C-NH_4OH-60**, while the products prepared in the presence of urea were denoted **E-urea-45** and **E-urea-60**, respectively.

4.3. Characterization. The structural features and phase purity of the synthesized CuO nanoparticles were investigated using an X-ray diffractometer (PANalytical X′-pert PRO-PW 3040/60) fitted with a Cu Kα (λ = 0.1541 nm) radiation source,a HORIBA Jobin-Yvon HR800 Raman microscope at room temperature and transmission electron microscope (Tecnai F20). XPS analyses were carried out using a PHI 5000 Versaprobe-scanning ESCA microprobe. A low-energy Ar^+ ion gun and low-energy neutralizer electron gun were used to minimize charging on the surface. Monochromatic Al Kα radiation ($h\nu$ = 1486.6 eV) was used as the excitation source. The morphology was characterized using a SEM (Zeiss). The optical emission properties were characterized at room temperature using a pulsed laser-PL spectrometer, equipped with a Kimmon He–Cd laser. The surface area and pore size distribution were analyzed using a N_2 adsorption–desorption isotherm (Micromeritics TRISTAR 300 surface area analyzer, USA). For magnetization measurements at low temperature, the VSM platform of a Dynacool facility was used (Quantum Design, USA). This platform enables measurement of magnetic moment to an accuracy of ±0.5% and with a noise rejection rate of better than 6H10^{-7} emu.

4.4. Fabrication and Analyses of Sensing Layer. The gas-sensing properties of the as-prepared CuO platelets powder were analyzed using a KSGAS6S gas testing station (Kenosistec, Italy). Figure 15 shows the schematic diagram of the gas testing station.

As we reported previously, prior to gas-sensing analyses, the sensing layers were fabricated by dispersing the as-prepared CuO powders in ethanol before it was drop-coated onto alumina substrates (containing a heater on the bottom side) and dried in an oven at 100 °C for 1 h. The average thickness of the sensing layers range between 15 and 20 μm (see the Supporting Information, Figure S3a,b).

DOI: 10.1021/acsomega.9b01882
ACS Omega 2019, 4, 18035–18048

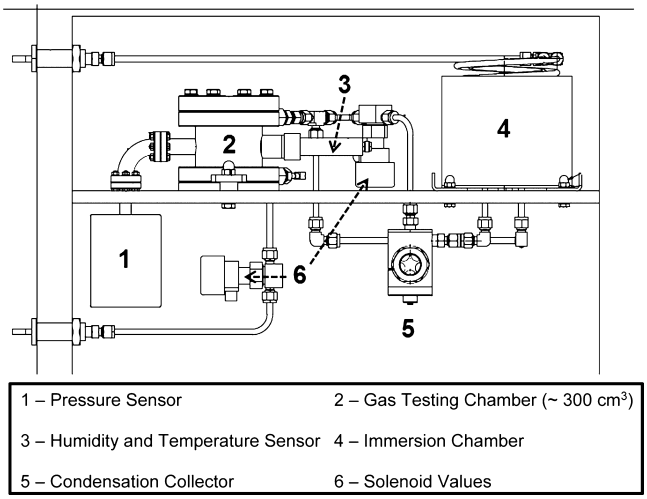

Figure 15. Schematic diagram of the gas testing station used during the gas-sensing analyses.

The fabricated sensors were placed in an airtight chamber and tested for sensitivity toward NH_3, CO, CH_4, NO_2, H_2S, and IPA gases at room temperature. The fabricated sensors were exposed to gas concentrations ranging from 5, 10 to 100 ppm with 10 ppm intervals. Dry air atmosphere (79% nitrogen and 21% oxygen, i.e., 0% relative humidity) and relative humidity (RH) of 10−60% conditions were used to conduct the measurements. The resistance of the device was measured using a Keithley 6487 picoammeter/voltage source meter.

■ ASSOCIATED CONTENT

Supporting Information

The Supporting Information is available free of charge on the ACS Publications website at DOI: 10.1021/acsomega.9b01882.

XRD data and Raman spectra, BET data and graphs, Hall-effect analyses data, and sensing layer and gas-sensing response of different CuO materials (PDF)

■ AUTHOR INFORMATION

Corresponding Author

*E-mail: oosthuizendn@gmail.com.

ORCID

Dina N. Oosthuizen: 0000-0001-8424-9353
David E. Motaung: 0000-0001-9888-6089
Hendrik C. Swart: 0000-0001-5233-0130

Notes

The authors declare no competing financial interest.

■ ACKNOWLEDGMENTS

We acknowledge the Department of Science and Technology (DST) and the Council for Scientific and Industrial Research (CSIR) for the financial support (project numbers: HGER27 and HGER61S). We acknowledge the University of Pretoria for the use of their Hall-Effect facilities for the measurements, Elizabeth Coetsee-Hugo and Lucas Erasmus for assistance with XPS and PL analyses, respectively, at University of the Free State, and the technical support of Me. S. Xhaka with the VSM analyses at the University of Johannesburg. Further financial support is acknowledged to the South African Research Chairs Initiative of the DST and the National Research Fund (NRF) (grant 84415).

■ REFERENCES

(1) (a) Overview of Greenhouse Gases. https://www.epa.gov/ghgemissions/overview-greenhouse-gases (accessed 01 06, 2018). (b) Burden of disease from the joint effects of Household and Ambient Air Pollution for 2012. http://www.who.int/airpollution/en/ (accessed 03 04, 2018). (c) Ambient air pollution: Pollutants. http://www.who.int/airpollution/ambient/pollutants/en/ (accessed 01 06, 2018).

(2) (a) Meth, O. New satellite data reveals the world's largest air pollution hotspot is Mpumalanga—South Africa. https://www.greenpeace.org/africa/en/press/4202/new-satellite-data-reveals-the-worlds-largest-air-pollution-hotspot-is-mpumalanga-south-africa/ (accessed 08 22, 2019). (b) Lourens, A. S. M.; Butler, T. M.; Beukes, J. P.; van Zyl, P. G.; Beirle, S.; Wagner, T. K.; Heue, K.-P.; Pienaar, J. J.; Fourie, G. D.; Lawrence, M. G. Re-evaluating the NO_2 hotspot over the South African Highveld. *S. Afr. J. Sci.* **2012**, *108*, 83−91. (c) Broken promises: The failure of the Highveld priority area. https://cer.org.za/programmes/pollution-climate-change/publications/broken-promises-the-failure-of-the-highveld-priority-area (accessed 28 11, 2017).

(3) Barsan, N.; Schierbaum, K., 1—Introduction. In *Gas Sensors Based on Conducting Metal Oxides*; Barsan, N., Schierbaum, K., Eds.; Elsevier, 2019; pp 1−11.

(4) Oprea, A.; Degler, D.; Barsan, N.; Hemeryck, A.; Rebholz, J., 3 - Basics of semiconducting metal oxide−based gas sensors. In *Gas Sensors Based on Conducting Metal Oxides*; Barsan, N., Schierbaum, K., Eds.; Elsevier, 2019; pp 61−165.

(5) (a) Zhang, J.; Zeng, D.; Zhu, Q.; Wu, J.; Huang, Q.; Xie, C. Effect of Nickel Vacancies on the Room-Temperature NO_2 Sensing Properties of Mesoporous NiO Nanosheets. *J. Phys. Chem. C* **2016**, *120*, 3936−3945. (b) Zhang, J.; Qin, Z.; Zeng, D.; Xie, C. Metal-oxide-semiconductor based gas sensors: screening, preparation, and integration. *Phys. Chem. Chem. Phys.* **2017**, *19*, 6313−6329. (c) Korotcenkov, G. Metal oxides for solid-state gas sensors: What determines our choice? *Mater. Sci. Eng. B* **2007**, *139*, 1−23. (d) Liu, L.; Shu, S.; Zhang, G.; Liu, S. Highly Selective Sensing of C_2H_6O, HCHO, and C_3H_6O Gases by Controlling SnO_2 Nanoparticle Vacancies. *ACS Appl. Nano Mater.* **2018**, *1*, 31−37. (e) Korotcenkov, G. The role of morphology and crystallographic structure of metal oxides in response of conductometric-type gas sensors. *Mater. Sci. Eng., R* **2008**, *61*, 1−39.

(6) (a) Majumder, D.; Roy, S. Development of Low-ppm CO Sensors Using Pristine CeO_2 Nanospheres with High Surface Area. *ACS Omega* **2018**, *3*, 4433−4440. (b) Zhang, Y.; Li, L.; Ao, S.; Wang, J.; Li, G. Interfacial Doping of Heteroatom in Porous SnO_2 for Highly Sensitive Surface Properties. *ACS Omega* **2018**, *3*, 6988−6997. (c) Nandi, A.; Nag, P.; Panda, D.; Dhar, S.; Hossain, S. M.; Saha, H.; Majumdar, S. Outstanding Room-Temperature Hydrogen Gas Detection by Plasma-Assisted and Graphene-Functionalized Core-Shell Assembly of SnO_2 Nanoburflower. *ACS Omega* **2019**, *4*, 11053−11065. (d) Han, X.; Han, X.; Li, L.; Wang, C. Controlling the morphologies of WO_3 particles and tuning the gas sensing properties. *New J. Chem.* **2012**, *36*, 2205−2208. (e) Vallejos, S.; Pizúrová, N.; Gràcia, I.; Sotelo-Vazquez, C.; Čechal, J.; Blackman, C.; Parkin, I.; Cané, C. ZnO Rods with Exposed {100} Facets Grown via a Self-Catalyzed Vapor-Solid Mechanism and Their Photocatalytic and Gas Sensing Properties. *ACS Appl. Mater. Interfaces* **2016**, *8*, 33335−33342.

(7) (a) Jain, S.; Patrike, A.; Badadhe, S. S.; Bhardwaj, M.; Ogale, S. Room-Temperature Ammonia Gas Sensing Using Mixed-Valent $CuCo_2O_4$ Nanoplatelets: Performance Enhancement through Stoichiometry Control. *ACS Omega* **2018**, *3*, 1977−1982. (b) Alali, K. T.; Lu, Z.; Zhang, H.; Liu, J.; Liu, Q.; Li, R.; Aljebawi, K.; Wang, J. P-p heterojunction $CuO/CuCo_2O_4$ nanotubes synthesized via electrospinning technology for detecting n-propanol gas at room temperature. *Inorg. Chem. Front.* **2017**, *4*, 1219−1230. (c) Zhang, J.; Zeng,

DOI: 10.1021/acsomega.9b01882
ACS Omega 2019, 4, 18035−18048

D.; Zhu, Q.; Wu, J.; Huang, Q.; Zhang, W.; Xie, C. Enhanced room temperature NO_2 response of NiO-SnO_2 nanocomposites induced by interface bonds at the p-n heterojunction. *Phys. Chem. Chem. Phys.* **2016**, *18*, 5386−5396. (d) Xing, R.; Sheng, K.; Xu, L.; Liu, W.; Song, J.; Song, H. Three-dimensional In_2O_3-CuO inverse opals: synthesis and improved gas sensing properties towards acetone. *RSC Adv.* **2016**, *6*, 57389−57395. (e) Dai, Z.; Lee, C.-S.; Tian, Y.; Kim, I.-D.; Lee, J.-H. Highly reversible switching from P- to N-type NO_2 sensing in a monolayer Fe_2O_3 inverse opal film and the associated P-N transition phase diagram. *J. Mater. Chem. A* **2015**, *3*, 3372−3381. (f) Oosthuizen, D. N.; Motaung, D. E.; Swart, H. C. In depth study on the notable room-temperature NO_2 gas sensor based on CuO nanoplatelets prepared by sonochemical method: Comparison of various bases. *Sens. Actuators, B* **2018**, *266*, 761−772. (g) Shafiei, M.; Hoshyargar, F.; Lipton-Duffin, J.; Piloto, C.; Motta, N.; O'Mullane, A. P. Conversion of n-Type CuTCNQ into p-Type Nitrogen-Doped CuO and the Implication for Room-Temperature Gas Sensing. *J. Phys. Chem. C* **2015**, *119*, 22208−22216. (h) Wang, Z.; Xiao, Y.; Cui, X.; Cheng, P.; Wang, B.; Gao, Y.; Li, X.; Yang, T.; Zhang, T.; Lu, G. Humidity-Sensing Properties of Urchinlike CuO Nanostructures Modified by Reduced Graphene Oxide. *ACS Appl. Mater. Interfaces* **2014**, *6*, 3888−3895. (i) Wang, C.; Cui, X.; Liu, J.; Zhou, X.; Cheng, X.; Sun, P.; Hu, X.; Li, X.; Zheng, J.; Lu, G. Design of Superior Ethanol Gas Sensor Based on Al-Doped NiO Nanorod-Flowers. *ACS Sens.* **2016**, *1*, 131−136. (j) Zhou, L.; Wang, S.; Xu, D.; Guo, Y. Impact of Mixing for the Production of CuO Nanoparticles in Supercritical Hydrothermal Synthesis. *Ind. Eng. Chem. Res.* **2014**, *53*, 481−493.

(8) (a) Henzler, K.; Heilemann, A.; Kneer, J.; Guttmann, P.; Jia, H.; Bartsch, E.; Lu, Y.; Palzer, S., Investigation of reactions between trace gases and functional CuO nanospheres and octahedrons using NEXAFS-TXM imaging. **2015**, *5*, 17729; DOI: 10.1038/srep17729 (b) Zhang, J.; Zeng, D.; Zhu, Q.; Wu, J.; Xu, K.; Liao, T.; Zhang, G.; Xie, C. Effect of Grain-Boundaries in NiO Nanosheet Layers Room-Temperature Sensing Mechanism under NO_2. *J. Phys. Chem. C* **2015**, *119*, 17930−17939.

(9) (a) Siddiqui, H.; Qureshi, M. S.; Haque, F. Z. Valuation of copper oxide (CuO) nanoflakes for its suitability as an absorbing material in solar cells fabrication. *Optik* **2016**, *127*, 3713−3717. (b) Volanti, D. P.; Orlandi, M. O.; Andrés, J.; Longo, E. Efficient microwave-assisted hydrothermal synthesis of CuO sea urchin-like architectures via a mesoscale self-assembly. *CrystEngComm* **2010**, *12*, 1696−1699.

(10) (a) Umar, A.; Lee, J.-H.; Kumar, R.; Al-Dossary, O.; Ibrahim, A. A.; Baskoutas, S. Development of highlysensitive and selective ethanol sensor based on lance-shaped CuO nanostructures. *Mater. Des.* **2016**, *105*, 16. (b) Yang, C.; Su, X.; Xiao, F.; Jian, J.; Wang, J. Gas sensing properties of CuO nanorods synthesized by a microwave-assisted hydrothermal method. *Sens. Actuators, B* **2011**, *158*, 299−303. (c) Yang, C.; Su, X.; Wang, J.; Cao, X.; Wang, S.; Zhang, L. Facile microwave-assisted hydrothermal synthesis of varied-shaped CuO nanoparticles and their gas sensing properties. *Sens. Actuators, B* **2013**, *185*, 159−165. (d) Yang, C.; Xiao, F.; Wang, J.; Su, X. 3D flower- and 2D sheet-like CuO nanostructures: Microwave-assisted synthesis and application in gas sensors. *Sens. Actuators, B* **2015**, *207*, 177−185. (e) Yin, M.; Liu, S. Synthesis of CuO microstructures with controlled shape and size and their exposed facets induced enhanced ethanol sensing performance. *Sens. Actuators, B* **2016**, *227*, 328−335. (f) Zhu, G.; Xu, H.; Xiao, Y.; Liu, Y.; Yuan, A.; Shen, X. Facile Fabrication and Enhanced Sensing Properties of Hierarchically Porous CuO Architectures. *ACS Appl. Mater. Interfaces* **2012**, *4*, 744−751. (g) Wang, Y.; Lü, Y.; Zhan, W.; Xie, Z.; Kuang, Q.; Zheng, L. Synthesis of porous Cu_2O/CuO cages using Cu-based metal-organic frameworks as templates and their gas-sensing properties. *J. Mater. Chem. A* **2015**, *3*, 12796−12803.

(11) (a) Bedi, R. K.; Singh, I. Room-Temperature Ammonia Sensor Based on Cationic Surfactant-Assisted Nanocrystalline CuO. *ACS Appl. Mater. Interfaces* **2010**, *2*, 1361−1368. (b) Breedon, M.; Spizzirri, P.; Taylor, M.; du Plessis, J.; McCulloch, D.; Zhu, J.; Yu, L.; Hu, Z.; Rix, C.; Wlodarski, W.; Kalantar-zadeh, K. Synthesis of Nanostructured Tungsten Oxide Thin Films: A Simple, Controllable, Inexpensive, Aqueous Sol−Gel Method. *Cryst. Growth Des.* **2010**, *10*, 430−439. (c) Li, Z.; Wang, N.; Lin, Z.; Wang, J.; Liu, W.; Sun, K.; Fu, Y. Q.; Wang, Z. Room-Temperature High-Performance H_2S Sensor Based on Porous CuO Nanosheets Prepared by Hydrothermal Method. *ACS Appl. Mater. Interfaces* **2016**, *8*, 20962−20968. (d) Cao, Y.; Liu, S.; Jian, X.; Zhu, G.; Yin, L.; Zhang, L.; Wu, B.; Wei, Y.; Chen, T.; Gao, Y.; Tang, H.; Wang, C.; He, W.; Zhang, W. Synthesis of high-purity CuO nanoleaves and analysis of their ethanol gas sensing properties. *RSC Adv.* **2015**, *5*, 34788−34794. (e) Brown, G. E.; Henrich, V. E.; Casey, W. H.; Clark, D. L.; Eggleston, C.; Felmy, A.; Goodman, D. W.; Grätzel, M.; Maciel, G.; McCarthy, M. I.; Nealson, K. H.; Sverjensky, D. A.; Toney, M. F.; Zachara, J. M. Metal Oxide Surfaces and Their Interactions with Aqueous Solutions and Microbial Organisms. *Chem. Rev.* **1999**, *99*, 77−174. (f) Volanti, D. P.; Felix, A. A.; Orlandi, M. O.; Whitfield, G.; Yang, D.-J.; Longo, E.; Tuller, H. L.; Varela, J. A. The Role of Hierarchical Morphologies in the Superior Gas Sensing Performance of CuO-Based Chemiresistors. *Adv. Funct. Mater.* **2013**, *23*, 1759−1766.

(12) Cullity, B. D. *Elements of X-ray diffraction*; Addison-Wesley Pub. Co.: Reading, Mass, 1956.

(13) (a) Liu, X.; Liu, G.; Wang, L.; Li, Y.; Ma, Y.; Ma, J. Morphology- and facet-controlled synthesis of CuO micro/nanomaterials and analysis of their lithium ion storage properties. *J. Power Sources* **2016**, *312*, 199−206. (b) Briggs, D. Handbook of X-ray Photoelectron Spectroscopy C. D., Wanger, W. M., Riggs, L. E., Davis, J. F., Moulder and G. E., Muilenberg Perkin-Elmer Corp., Physical Electronics Division: Eden Prairie, Minnesota, USA, 1979. 190 pp. $195. *Surf. Interface Anal.* **1981**, *3*, v. (c) Son, D. I.; You, C. H.; Kim, T. W. Structural, optical, and electronic properties of colloidal CuO nanoparticles formed by using a colloid-thermal synthesis process. *Appl. Surf. Sci.* **2009**, *255*, 8794−8797. (d) Anandan, S.; Lee, G.-J.; Wu, J. J. Sonochemical synthesis of CuO nanostructures with different morphology. *Ultrason. Sonochem.* **2012**, *19*, 682−686. (e) Tamuly, C.; Saikia, I.; Hazarika, M.; Das, M. R. Reduction of aromatic nitro compounds catalyzed by biogenic CuO nanoparticles. *RSC Adv.* **2014**, *4*, 53229−53236.

(14) Klinbumrung, A.; Thongtem, T.; Thongtem, S. Characterization and gas sensing properties of CuO synthesized by DC directly applying voltage. *Appl. Surf. Sci.* **2014**, *313*, 640−646.

(15) Dupin, J.-C.; Gonbeau, D.; Vinatier, P.; Levasseur, A. Systematic XPS studies of metal oxides, hydroxides and peroxides. *Phys. Chem. Chem. Phys.* **2000**, *2*, 1319−1324.

(16) Chang, S.-S.; Lee, H.-J.; Park, H. J. Photoluminescence properties of spark-processed CuO. *Ceram. Int.* **2005**, *31*, 411−415.

(17) Li, Z.; Li, H.; Wu, Z.; Wang, M.; Luo, J.; Torun, H.; Hu, P.; Yang, C.; Grundmann, M.; Liu, X.; Fu, Y. Advances in designs and mechanisms of semiconducting metal oxide nanostructures for high-precision gas sensors operated at room temperature. *Mater. Horiz.* **2019**, *6*, 470−506.

(18) Mhlongo, G. H.; Shingange, K.; Tshabalala, Z. P.; Dhonge, B. P.; Mahmoud, F. A.; Mwakikunga, B. W.; Motaung, D. E. Room temperature ferromagnetism and gas sensing in ZnO nanostructures: Influence of intrinsic defects and Mn, Co, Cu doping. *Appl. Surf. Sci.* **2016**, *390*, 804−815.

(19) Korotcenkov, G.; Cho, B. K. Instability of metal oxide-based conductometric gas sensors and approaches to stability improvement (short survey). *Sens. Actuators, B* **2011**, *156*, 527−538.

(20) Barsan, N.; Weimar, U. Conduction Model of Metal Oxide Gas Sensors. *J. Electroceram.* **2001**, *7*, 143−167.

(21) (a) Korotcenkov, G.; Brinzari, V.; Pronin, I. A.; Ham, M. H.; Cho, B. K. Metal Oxides for Application in Conductometric Gas Sensors: How to Choose? *Solid State Phenom.* **2017**, *266*, 187−195. (b) Lee, J.-H. Gas sensors using hierarchical and hollow oxide nanostructures: Overview. *Sens. Actuators, B* **2009**, *140*, 319−336. (c) Pokhrel, S.; Simion, C. E.; Quemener, V.; Bârsan, N.; Weimar, U. Investigations of conduction mechanism in Cr_2O_3 gas sensing thick

DOI: 10.1021/acsomega.9b01882
ACS Omega 2019, 4, 18035−18048

films by ac impedance spectroscopy and work function changes measurements. *Sens. Actuators, B* **2008**, *133*, 78−83.
(22) (a) Sun, X.; Hu, X.; Wang, Y.; Xiong, R.; Li, X.; Liu, J.; Ji, H.; Li, X.; Cai, S.; Zheng, C. Enhanced Gas-Sensing Performance of Fe-Doped Ordered Mesoporous NiO with Long-Range Periodicity. *J. Phys. Chem. C* **2015**, *119*, 3228−3237. (b) Sänze, S.; Hess, C. Ethanol Gas Sensing by Indium Oxide: An Operando Spectroscopic Raman-FTIR Study. *J. Phys. Chem. C* **2014**, *118*, 25603−25613. (c) Yamazoe, N. New approaches for improving semiconductor gas sensors. *Sens. Actuators, B* **1991**, *5*, 7−19.
(23) Kim, K.-M.; Jeong, H.-M.; Kim, H.-R.; Choi, K.-I.; Kim, H.-J.; Lee, J.-H. Selective Detection of NO_2 Using Cr-Doped CuO Nanorods. *Sensors* **2012**, *12*, 8013.
(24) Oosthuizen, D. N.; Motaung, D. E.; Swart, H. C. Selective detection of CO at room temperature with CuO nanoplatelets sensor for indoor air quality monitoring manifested by crystallinity. *Appl. Surf. Sci.* **2019**, *466*, 545−553.

DOI: 10.1021/acsomega.9b01882
ACS Omega 2019, 4, 18035−18048